# Magnetic field-modulated plasmonic scattering of hybrid nanorods for FFT-weighted OCT imaging in NIR-II

*Zhiwei Li[1‡†], Wesley Poon[2‡], Zuyang Ye[1], Fenglian Qi[1], Boris Hyle Park[2*], and Yadong Yin[1*]*

[1]Department of Chemistry, University of California, Riverside, CA 92521, USA.

Email: yadong.yin@ucr.edu

[2]Department of Bioengineering, University of California Riverside, CA 92521, USA

Email: hylepark@engr.ucr.edu

ABSTRACT: We report a method for FFT-weighted optical coherence tomography (OCT) in the second biological tissue transparency window by actively modulating the plasmonic scattering of $Fe_3O_4$@Au hybrid nanorods using magnetic fields. Instead of tracking the nanoparticles' lateral displacement in conventional magnetomotive OCT imaging, we monitor the nanorod rotation and optical signal changes under an alternating magnetic field in real time. The coherent rotation of the nanorods with the field produces periodic OCT signals, and the Fast Fourier transform (FFT) is then used to convert the periodic OCT signals in the time domain to a single peak in the frequency domain. This allows automatic screening of nanorod signals from the random biological noises and reconstruction of FFT-weighted images using a computer program based on a time-sequence image set. Compared with conventional magnetomotive OCT, the FFT-weighted imaging technique creates enhanced OCT images with dB-scale contrast over an order of magnitude higher than the original images.

KEYWORDS: optical coherence tomography, background-free imaging, $Fe_3O_4$@Au hybrid nanorods, fast Fourier transform, plasmonic scattering, magnetic tuning

Optical coherence tomography (OCT) is an optical imaging technique for acquiring sub-surface images of tissues and organs at a near-microscopic resolution,[1] about two orders of magnitude finer than ultrasound imaging.[2, 3] It collects and processes a small portion of an incident optical beam scattered from biological tissues for tissue morphological tomography.[4] OCT allows *in situ* imaging of fine structures of tissues in real time based on inherent contrast from the heterogeneity of optical refractive index, without the need for complicated treatment of specimens as in conventional excisional biopsy and histopathology.[5] As a noninvasive imaging technique, OCT has been extensively studied in academic research and widely used in clinical applications for ophthalmology,[6] diagnosing cancer,[7] imaging tissue pathology,[8] and guiding surgical procedures.[9-11]

While the ability of OCT to generate cross-sectional images without contrast agents is often regarded as a primary strength of the technique, there are occasions where identification of select regions through a contrast agent is desired. Active contrast agents have thus been introduced to enhance image quality,[12, 13] which can change their properties in response to external stimuli, such as heat, light, and magnetic field.[14-18] Magnetomotive OCT, for example, takes advantage of the dynamic responses of magnetic particles to magnetic fields for imaging contrast.[19] The lateral displacement of magnetic particles or rotation of anisotropic magnetic nanostructures under applied magnetic fields induces stresses within the viscoelastic biological medium, creating locoregional scattering changes for imaging contrast.[19, 20] Suppression of non-contrast agent background can be achieved by pixel-subtraction between actively modulated OCT images.[21, 22]

The use of magnetic particles also enables multimodal imaging, such as magnetic resonance image (MRI) and magnetic particle imaging, and synergistic cancer treatment by magnetothermal therapy.[23-25] However, magnetomotive OCT is facing a few challenges during its development. First, the reversible lateral displacement and retrieval of magnetomotive signals are highly reliant on the restoring force of the elastic tissue so that its imaging performance is attenuated by the pathophysiological heterogeneity of tissues and inter-patient variations of tissue elasticity.[26-28] Second, in most cases, magnetic nanoparticles need to be first labeled on cells or functionalized by biological molecules for strong particle-tissue interactions, considerably large displacement, and detectable optical changes under magnetic fields.[15] Besides, with the pixel-subtraction method, it is difficult to completely eliminate the non-contrast agent background, which is referred to as background noise or biological noise because the OCT intensity back-reflected from biological tissues is not static instead fluctuates randomly.[19, 29] The pixel subtraction also reduces the signals from the target tissues or tumors, resulting in a limited enhancement in signal-to-noise ratio (SNR).

To overcome these challenges, we have developed a magnetic field-modulated, FFT-weighted OCT imaging technique that can completely remove any random and static background noises and significantly enhance the signal-to-noise ratio. Instead of tracking the lateral displacement of magnetic particles in conventional magnetoactive imaging,[30, 31] we monitor the periodic signal of plasmonic excitation of $Fe_3O_4$@Au nanorods under an alternating magnetic field to enable an FFT intensity-weighted imaging. $Fe_3O_4$@Au hybrid nanorods are synthesized using a seed-mediated, space-free confined growth method. The shape anisotropy of the $Fe_3O_4$ cores allows actively tuning the collective orientation of rods and efficiently modulating their optical scattering and plasmonic excitation using magnetic fields. With these nanorods as active contrast

agents, a time-sequence image set can be acquired by applying an alternating magnetic field. The periodic signals of the nanorods in the time domain are converted into a sharp peak in the frequency domain by FFT and can therefore be distinguished from the random OCT signals of background noises. A computer program is developed to automatically screen OCT signals of contrast agents and reconstruct FFT-weighted images. Simply extending the strategy to a volume scan can produce three-dimensional (3D) FFT-weighted volume rendering with greatly enhanced specificity and contrast.

## RESULTS AND DISCUSSION

**Preparation of $Fe_3O_4$@Au Hybrid Nanorods.** Superparamagnetic $Fe_3O_4$ nanorods were prepared by reducing pre-synthesized FeOOH nanorods (200 nm × 30 nm, **Fig. 1a**) using a surface-protected polyol process.[32, 33] Their surface was modified with (3-Aminopropyl)triethoxysilane, which allowed further attachment of Au seeds through electrostatic interaction.[34] Resorcinol (R) and formaldehyde (F) were polymerized in the presence of ammonia, forming a crosslinked resin shell wrapping the nanorods.[35, 36] Then, Au nanoshells could be homogeneously grown at the hard-soft interfaces between $Fe_3O_4$ cores and deformable RF shells (**Fig. s1**). This synthetic strategy uses $Fe_3O_4$/Au seeds@RF as templates, and the Au seeds are homogeneously distributed at the interfaces. Seeded growth is possible at the interfaces because the external RF shells are deformable, which allows successive deposition of reduced Au atoms along the lateral directions while limiting the Au growth along the radial directions. Such a sequence of events produces smooth Au nanoshells at the $Fe_3O_4$-RF interfaces. As shown in the TEM image in **Fig. 1b**, magnetic cores are completely covered by 25-nm Au nanoshells, forming $Fe_3O_4$@Au@RF hybrid nanorods. Interestingly, switching the direction of the applied magnetic field can actively modulate the plasmonic excitation of Au nanoshells due

to the magnetic anisotropy and strong responses of $Fe_3O_4$ nanorods.[37-39] Under ordinary light (**Fig. s2**), only transverse mode at 615 nm was excited when applying a parallel magnetic field, while an enhancement of longitudinal mode was observed under a perpendicular magnetic field.[40] The extinction spectra could be magnetically modulated over a broader range under polarized light, with the color of the solutions changing between blue and green. As shown in **Fig. 1c**, the extinction of longitudinal mode could be enhanced by 7 times when $Fe_3O_4$@Au@RF were aligned from parallel to perpendicular configuration. Such large tunability enables instant, reversible modulation of the optical properties.[41, 42] However, the spectra of FeOOH@Au nanorods showed negligible changes in response to external magnetic fields (**Fig. s3**) due to the lack of magnetic properties. To quantify the orientation-excitation correlation, we calculated optical cross-sections of nanorods under various orientations (inset in **Fig. 1d**). In **Fig. 1d**, the longitudinal peak intensity decreased, and the transverse peak intensity increased when $Fe_3O_4$@Au nanorods were aligned from $0^o$ to $90^o$ relative to light polarization, consistent with the measured spectra. In addition, we recognize ~80 % scattering contribution to the longitudinal extinction and ~50% scattering contribution to the transverse extinction (**Fig. s4**). The peak intensity of longitudinal and transverse modes has $\cos^2$- and $\sin^2$-dependence on the orientation of the nanorods, respectively (**Fig. s5a**).[43, 44] The scattering-dominated longitudinal mode is highly desirable for OCT imaging.[45] The calculated electric field distribution further confirms that the longitudinal excitation creates a dipole plasmon mode at 1250 nm and a hybridized mode at 575 nm, while the transverse excitation leads to a quadrupole mode at 575 nm and a hybridized mode at 650 nm (**Fig. s5b**). The hybridized modes represent the hybridization of the primitive plasmons of a solid Au spheroid and an ellipsoidal cavity inside a continuous Au matrix.[40]

**Magnetic Field-Modulated OCT Signals.** We first performed OCT imaging on the colloidal dispersion of nanorods. In a conventional OCT setup as shown in **Fig. s6**, a rotating magnetic field was applied during acquiring OCT images to control the nanorod alignment in solutions and biological tissues. The application of the magnetic field and the alignment of nanorods relative to the direction of incident light are further illustrated in **Fig. 2a**. As shown in **Fig. 2b**, water is near-transparent to light at 1300 nm due to the low scattering in the NIR-II window.[46] In the colloidal dispersion of nanorods, we observed strong scattering signals with a gradual decay in intensity along the image depth (**Fig. 2b**). As the beam is incident along the surface normal of the water-air interface, its intensity is attenuated by the scattering of homogenously dispersed nanorods. More interestingly, OCT signals could be immediately and reversibly modulated when external magnetic fields were applied (**Fig. s7 and supporting video 1**). The OCT signal was reduced when a parallel magnetic field ($B_{\parallel}$) was applied, as inferred from the following two observations. First, image contrast and SNR decreased at the water-air interface (**Fig. 2c**). Second, the image contrast gradient decreased in depth with better beam penetration when parallel magnetic fields were applied (**Fig. 2c**), indicating a decrease in nanorods scattering so that the incident beam could reach deeper regions. When the magnetic field was switched to perpendicular configuration ($B_{\perp}$), the OCT signals could be significantly enhanced. Our real-time measurement in **Fig. 2d** further elucidates that OCT signals of $Fe_3O_4$@Au@RF nanorods could be reversibly, rapidly, and remotely modulated by controlling the direction of magnetic fields. The SNR of OCT images could be regulated between ~25 dB and ~65 dB, while its decay rate along depth could be regulated between -70 dB/mm and -5 dB/mm. In comparison, the OCT signals and decay rate of FeOOH@Au@RF exhibited random fluctuation under the same measurement conditions due to the lack of magnetic response (**Fig. 2e**). With these

considerations, we conclude that $Fe_3O_4$@Au@RF nanorods are an ideal OCT contrast agent due to the scattering-dominated extinction of Au nanoshells. Their OCT signals changed within ± 40% of measured signals without an external magnetic field (**Fig. 2f**).

**In Vitro OCT Imaging by Pixel Subtraction.** We then used an artificial model to investigate *ex vivo* OCT imaging in NIR-II. As depicted in **Fig. 3a**, two capillary tubes were implanted into pork that mimicked biological noise in OCT imaging. Magnetically responsive $Fe_3O_4$@Au@RF nanorods were injected into the left capillary tube as the positive imaging contrast agent and FeOOH@Au@RF nanorods into the right as a negative control. A parallel and perpendicular magnetic field was applied in sequence during OCT imaging. As shown in **Fig. 3b**, the biological noises from pork tissues and the negative control only exhibited random signal fluctuation under different magnetic fields. In contrast, we observed a contrast increase in regions containing $Fe_3O_4$@Au@RF nanorods when a perpendicular magnetic field was applied. Recognizing the differences between the sequential images, we applied pixel-wise data processing to create background-free OCT images. It was achieved by subtracting the pixel intensity of the "$B_{\parallel}$" image from that of the "$B_{\perp}$" image. The reconstructed image in **Fig. 3b** shows that signals from both biological and synthetic backgrounds were removed, leaving some random signals in the OCT images. The parallel comparison of these OCT signal changes in **Fig. 3c** reveals a clear contrast enhancement for $Fe_3O_4$@Au@RF nanorods. Comparing the SNR before and after data processing showed a 400-fold enhancement in OCT imaging (**Fig. 3d**).

The above strategy can be extended to 3D OCT imaging. In a typical imaging methodology, 2D normal B-scan images were acquired twice in the same imaging region while parallel and magnetic fields were applied in sequence to modulate the optical signals. Pixel subtraction was performed between the two "$B_{\parallel}$" and "$B_{\perp}$" OCT images of the same cross-section. The "$B_{\parallel}$",

"$B_{\perp}$", and 3D volume rendering of the OCT images were shown in the left, middle, and right panels in **Fig. s8,** respectively. We found that all the signals from the responsive and nonresponsive nanorods were interfered with by the background noises, making it challenging to analyze the regions of interest (**Fig. 3e**). However, with the above data processing method, we could reconstruct 3D background-free OCT images based on the volume rendering of the subtracted 2D images (**Fig. 3f**). The capillary tube can be fully recovered, and both the biological and synthetic background noises were removed.

In addition to the phantom model, we now consider an *in vitro* model by injecting the contrast agent into pork tissue. The rotational resistance in biological tissue is much higher than in water, making coherent modulation of nanorods orientation more difficult.[47] Besides, the random diffusion of nanorods inside biological tissues could attenuate the imaging intensity due to the diluting effect.[48] To further demonstrate the feasibility of $Fe_3O_4$@Au@RF nanorods as active contrast agents, the magnetic and nonmagnetic nanorods were injected into the right and left sides of the pork, respectively (**Fig. 4a**). Perpendicular and parallel magnetic fields relative to light incidence were used to modulate the OCT signals of the nanorods. **Fig. 4b** shows the 2D B-scan images taken with magnetic fields of different orientations. We observed enhanced OCT signals in the area injected with $Fe_3O_4$@Au@RF nanorods but no changes on the right side containing the FeOOH@Au@RF nanorods. However, specifying the imaging areas of interest is impossible from single images (left and middle panels of **Figs. 4a** and **4b**) as the signals from the imaging contrast agent are mixed with background noises. This issue could be successfully addressed with pixel-wise data processing, and OCT images could be created by the differentiated pixels (right panel in **Fig. 4b**). We further reconstructed the 3D volume where the

noises from biological backgrounds could be removed (**Fig. 4c**). Besides, in the merged 3D reconstruction, the nanorods' signals could be easily recognized (**Fig. 4d**).

**Magnetic Field-Modulated, FFT-weighted OCT Imaging.** While the pixel-subtraction method can reduce background OCT noises, it is difficult to remove all noises completely due to their random fluctuation (as evidenced by the random noises after pixel subtraction in **Fig. 3b**).[49] To solve this problem, we introduced an FFT-processed OCT imaging that could entirely remove any noises. A time-sequence B-scan was performed in a PDMS model with two pre-designed channels, which were injected with $Fe_3O_4$@Au@RF nanorods. The nonresponsive FeOOH@Au@RF nanorods were first mixed in the PDMS model to serve as OCT noises. A typical image sequence in **Fig. 5a** demonstrated apparent contrast changes in the channel sections and random fluctuation in the background. When signals from representative sections (**Fig. 5b**) were analyzed, we observed periodic signals from the nanorods and random noises from the PDMS and surrounding air (**Fig. 5c**). Within 25 s, the nanorod signals remained coherent and periodic in accordance with the applied magnetic field due to the strong and fast magnetic responses of $Fe_3O_4$@Au@RF nanorods. FFT of these signals in the time domain led to a sharp and narrow peak for nanorod signals but only flat backgrounds for the random OCT signals in PDMS and air (**Fig. 6a**). When the frequency of an applied magnetic field increased from 1 Hz to 6 Hz, we observed a coherent increase in the FFT frequency (**Fig. 6b**), demonstrating the perfect magnetic response of the $Fe_3O_4$@Au@RF nanorods over a broad frequency. The FFT frequency is precisely twice the applied frequency, with a perfect linear dependence in the measurement (**Fig. 6c**). Such a simple correlation facilitates signal recognition in background-free imaging. As a magnetic field rotates 360$^o$ in one cycle, the longitudinal or transverse modes are excited twice because the nanorods have a two-fold rotational symmetry.

**Fig. 6d** shows one representative background-free OCT image after FFT processing (See Supplementary Information for detailed data processing). The background noises were removed entirely, creating well-delineated, highly specific images associated with nanorods. A 3D volume rendering could be achieved by simply applying the same data processing to each tomography image of a time-sequence image set (**Fig. 6e** and **supporting video 2**). The nanorod signals can be automatically screened and recognized, and any random or static noises could be easily distinguished in three dimensions. One additional advantage of the FFT-weighted imaging technique is that it can greatly enhance the SNR of the contrast agent, with dB-scale contrast of more than one order of magnitude higher than original OCT images (**Fig. 6f**). Notably, the FFT-processed imaging technique has a much more significant SNR enhancement, with a six-fold increase, than the pixel-based subtraction method in conventional magnetomotive OCT imaging (**Fig. 3d**). Such a significant improvement in SNR is attributed to three reasons: i) the strong magnetic responses and the optimal, scattering-dominated plasmonic properties of the $Fe_3O_4$@Au@RF nanorods; ii) the optical signal tracking of rotating nanorods with higher sensitivity than the lateral displacement in conventional magnetomotive OCT imaging; iii) the FFT-weighted signal processing that can efficiently recognize the specific signals from contrast agents and create background-free images based on the periodicity instead of the intensity of the original OCT signals.

We used an in vitro model to demonstrate the background-free imaging technique by injecting the $Fe_3O_4$@Au@RF nanorods into pork tissue. As shown in **Fig. 7a** and **supporting video 3**, a time-sequence OCT B-scan was acquired, with red arrows indicating the injected sites. To illustrate the FFT-processing, we specified signals from the injection areas (red rectangle in **Fig. 7b**) and also plotted signals from background tissues (blue rectangle) and air (green rectangle) in

**Fig. 7c**. The signals from injected areas (indicated by the red curve) were highly periodic with a much wider modulation range of ~10 dB than the ~ 1dB fluctuation range of tissue and air noises. Notably, although the tissue noise intensity was significantly higher than the OCT intensity of nanorods signals (blue and red curves in **Fig. 7c**), the latter could be easily recognized by the sharp and defined peak in the frequency-domain curve (**Fig. 7d**), further underpinning the advantages of FFT processing in recognizing any periodic signals without being limited by signal intensity. By carrying out the FFT-processed imaging for pixels of each image in a time-sequence image set (**Fig. s9**), we show the 3D rendering of injected nanorods, background biological tissue, and merged images in **Figs**. **7e**, **7f**, and **7g**, respectively. These 3D reconstructed images clearly demonstrated that specific nanorod signals could be identified, and background-free images could be created by the proposed FFT-weighted data processing. Additionally, simple measurements of the signal intensity before and after data processing indicate over 10-folds enhancement in SNR (**Fig. 7h**). The initial OCT image has a negative value of SNR because the signal intensity in background tissue is much higher than that of nanorods.

## CONCLUSION

In conclusion, we have developed a reliable and robust strategy for background-free OCT imaging in the second NIR window. At the heart of this strategy is a smart imaging contrast agent, magnetic/plasmonic hybrid nanorods synthesized using an unconventional seed-mediated confined growth method, with actively tunable scattering in response to the direction changes of the applied magnetic field. Thanks to their magnetic $Fe_3O_4$ nanorod cores and plasmonic Au nanoshells, the hybrid nanorods can produce magnetically modulated OCT signals in an instant, remote, and reversible manner, enabling the development of a magnetic field-modulated, FFT-

processed OCT imaging. This FFT intensity-weighted imaging technique can reliably recognize the periodic signals of magnetic nanorods under an alternating magnetic field over a broad frequency range, diminish any random noises from the backgrounds, and create background-free images with greatly enhanced SNR. Compared with conventional magnetomotive imaging technique and pixel subtraction method, the current imaging technique features several advantages, including faster responses due to the highly sensitive tracking of the nanorods' optical signals under rotating magnetic fields, greater enhancement of SNR and image contrast ascribed to the FFT intensity-weighted imaging, and the complete removal of any random or stationary noises. We believe that the smart contrast agent developed in this work and the proposed imaging technique hold great promise for practical 2D and 3D OCT imaging with high contrast, resolution, and specificity.

## EXPERIMENTAL SECTION

**Synthesis of FeOOH nanorods.** The β-FeOOH rods (200 nm in length and 30 nm in width) were synthesized using a hydrolysis method. Typically, aqueous $FeCl_3$ solution (40 mM, 4 L) is reacted for two months at room temperature.[50, 51] Simply increasing the reaction time increases rod size. For example, prolonging the reaction to six months produces rods with a length of 322 nm and a width of 70 nm.

**Surface-protected reduction of FeOOH nanorods.** First, FeOOH was modified by polyacrylic acid (PAA). Typically, 3 mL of FeOOH (90 mg/mL) was added into 120 mL of water containing 43.2 mg of PAA. The solution was magnetically stirred overnight. FeOOH was recovered by centrifugation and washed with distilled (DI) water three times at 11000 rpm for 5 min. The FeOOH-PAA was dispersed in minimal water (~ 50 μL). FeOOH-PAA was reduced to magnetic

nanorods in diethylene glycol (DEG) at 220 ºC.[33] 15 mL of DEG was heated to 220ºC under nitrogen flow, to which FeOOH-PAA aqueous solution was injected at a high temperature. The reduction takes 6 h under nitrogen protection. The final product was washed with ethanol and water three times and dispersed in 9 mL water.

**Cystamine modification of magnetic nanorods.** 3 mL of $Fe_3O_4$ nanorod dispersion was added to 10 mL of cystamine solution (1 mg/mL). The mixture was magnetically stirred overnight. The magnetic nanorods were washed three times by water and then dispersed in 3 mL of DI water.

**Au seed preparation.** The Au seeds were prepared according to a previously reported method.[34] To 45 mL of MilliQ water, 12 uL of Tetrakis(hydroxymethyl)phosphonium chloride (THPC) and 250 µL of NaOH (2M) were added. After 5 min, 2 mL $HAuCl_4$ (1%) was added. The solution was covered with foil and stirred overnight. Afterward, it was stored at 4 ºC as a stock seed solution.

**Au seed attachment and PVP modification.** 3 mL of magnetic nanorods in water was added into 20 mL of Au seed stock solution. The mixture was stirred for about 1 h. Excess Au seeds were discarded after centrifugation at 11000 rpm for 10 min. Afterward, 5 mL of DI water was added to disperse the solids. It was then transferred to 10 mL of PVP solution (20 mg/mL, molecular weight=10000) under sonication for surface modification. The mixture was stirred overnight at room temperature. Excess PVP was removed by centrifuge at 14500 rpm for 10 min. The solids were washed with DI water three times and finally dispersed in 28 mL of MilliQ water.

**RF coating.** To a 28 mL above solution containing 78.2 mg $Fe_3O_4$, 20 mg of R and 28 µL of F were added into that dispersion sequentially. After that, the mixture was heated to 50ºC, and then

100 μL ammonium solution (2.8%) was added quickly. The reactive was kept at 50°C for 2 hrs and heated to 100 °C. The condensation at 100 °C took 5 hrs. The final product was washed with Milli Q water three times and dispersed in 2 mL Milli Q water as seed solution. The thickness of RF can be easily tuned by adjusting the amount of R and F. In a typical process, 28 μL of F was added for each 20 mg of R.

**Confined growth of FeOOH@Au@RF and $Fe_3O_4$@Au@RF nanorods.** In a typical process to prepare $Fe_3O_4$@Au@RF nanorods, 500 μL of PVP (50mg/mL, molecular weight=40000), 100 μL of NaOL (10 mM), 20 μL of $HAuCl_4$ (0.25 M) and 50 μL of $H_2O_2$ were added into 7.5 mL of deionized water in sequence. Then, 50 μL of $Fe_3O_4$/Aus@RF solution was added. The reaction occurred at room temperature for 30 min. The product was washed with deionized water three times and dispersed in deionized water for characterization. The preparation of FeOOH@Au@RF nanorods is the same as the preparation of $Fe_3O_4$@Au@RF nanorods. The only difference is that the FeOOH nanorods are directly used for cystamine modification without being reduced after PAA modification. The amount of FeOOH, PAA, Au seeds, cystamine, R, and F is the same as that used in preparing $Fe_3O_4$@Au@RF.

**OCT imaging setup.** The magnetic field-modulated, FFT-weighted OCT imaging was performed in a conventional OCT facility. The detailed setup information is shown in **Fig. s6**.

**Magnetic field-modulated, FFT-weighted OCT imaging.** OCT images in **Figs. 2b**, **3**, and **4**, used for pixel subtraction in producing background-free imaging, were acquired under magnetic fields of different directions as indicated in the individual panel. In these experiments, $B_\perp$ and $B_\parallel$ represent static magnetic fields perpendicular and parallel to the directions of the incident light, respectively. A magnet with a cubic shape was used to control the alignment of the nanorods for

both ex vivo and in vitro OCT imaging, as shown in these Figures. For FFT-weighted OCT imaging, a rotating magnetic field with controllable rotating frequency was needed to obtain a time-sequence image set. In experiments, a magnetic stirring plate was used underneath models (**Fig. 5**) and biological tissues (**Fig. 7**) to acquire videos in a conventional OCT setup. The image set used for FFT was derived from the videos when the rotating frequency of the stirring plate was precisely controlled. For OCT imaging in biological tissues, the nanorods were directly injected into the tissues.

**Calculation of SNR.** SNR of intensity is calculated by first calculating an average of OCT intensity in dB from a selected region of a frame in the air above the sample representing the background noise of data acquisition. Then, this mean value representing the noise floor (in dB) is subtracted from all points in the image. Because dB is a logarithmic value, this represents a ratio of the raw measured OCT signal intensity, hence, "SNR." SNR of FFT values is similar in concept; however, the noise floor after FFT is much less than 1 due to noise being random in nature and therefore not having a strong frequency component matching the frequency of variation (in other words, double the frequency of magnetic field rotation). Hence, the signal value at the expected frequency after FFT tends to be much lower than 1 and approaches 0. Converting these FFT values to dB is calculated as 10*log(FFT).

ASSOCIATED CONTENT

**Supporting Information**.

The Supporting Information is available free of charge.

Figures S1-S9, with additional experimental results (PDF).

Move S1: OCT signals of a nanorod dispersion under an alternating magnetic field (avi).

Move S2: 3D rendering of the FFT-weighted OCT images (avi).

Move S3: Responsive OCT signals of nanorods in biological tissues under an alternating magnetic field (avi).

AUTHOR INFORMATION

**Corresponding Author**

B. Hyle Park - Department of Bioengineering, University of California Riverside, CA 92521, USA; Email: hylepark@engr.ucr.edu

Yadong Yin - Department of Chemistry, University of California, Riverside, CA 92521, USA; Email: yadong.yin@ucr.edu

**Present Addresses**

†Department of Chemistry and International Institute for Nanotechnology, Northwestern University, 2145 Sheridan Road, Evanston, IL, 60208 USA

**Author Contributions**

The manuscript was written with the contributions of all authors. All authors have approved the final version of the manuscript. ‡These authors contributed equally.

**Funding Sources**

U.S. National Science Foundation (CHE-1808788) and the seed funding through the Committee on Research (CoR) Grant from the UCR Academic Senate.

**Notes**

The authors declare no competing financial interest.

**Acknowledgments:**

The authors are grateful for the financial support from the U.S. National Science Foundation (CHE-1808788). Yin also thanks the UCR Academic Senate for providing the seed funding through the Committee on Research (CoR) Grant.

**References**

1. Marques, M. J.; Green, R.; King, R.; Clement, S.; Hallett, P.; Podoleanu, A., Sub-surface Characterisation of Latest-generation Identification Documents Using Optical Coherence Tomography. *Sci. Justice* **2021,** *61*, 119-129.
2. Fujimoto, J. G., Optical Coherence Tomography for Ultrahigh Resolution In Vivo Imaging. *Nat. Biotechnol.* **2003,** *21*, 1361-1367.
3. Drexler, W.; Morgner, U.; Kärtner, F.; Pitris, C.; Boppart, S. A.; Li, X.; Ippen, E.; Fujimoto, J., In Vivo Ultrahigh-resolution Optical Coherence Tomography. *Opt. Lett.* **1999,** *24*, 1221-1223.
4. Tearney, G.; Brezinski, M.; Southern, J.; Bouma, B.; Boppart, S. A.; Fujimoto, J., Optical Biopsy in Human Gastrointestinal Tissue Using Optical Coherence Tomography. *Am. J. Gastroenterol.* **1997,** *92,* 1800-1804.
5. Fujimoto, J. G.; Brezinski, M. E.; Tearney, G. J.; Boppart, S. A.; Bouma, B.; Hee, M. R.; Southern, J. F.; Swanson, E. A., Optical Biopsy and Imaging Using Optical Coherence Tomography. *Nat. Med.* **1995,** *1*, 970-972.
6. Fujimoto, J. G.; Drexler, W.; Schuman, J. S.; Hitzenberger, C. K., Optical Coherence Tomography (OCT) in Ophthalmology: Introduction. *Opt. Express* **2009,** *17*, 3978-3979.
7. Zeng, Y.; Xu, S.; Chapman, J. W.; Li, S.; Alipour, Z.; Abdelal, H.; Chatterjee, D.; Mutch, M.; Zhu, Q., Real-time Colorectal Cancer Diagnosis Using PR-OCT with Deep Learning. *Theranostics* **2020,** *10*, 2587-2596.
8. Chiu, S. J.; Izatt, J. A.; O'Connell, R. V.; Winter, K. P.; Toth, C. A.; Farsiu, S., Validated Automatic Segmentation of AMD Pathology Including Drusen and Geographic Atrophy in SD-OCT Images. *Invest. Ophthalmol. Vis. Sci.* **2012,** *53*, 53-61.
9. Vakoc, B. J.; Fukumura, D.; Jain, R. K.; Bouma, B. E., Cancer Imaging by Optical Coherence Tomography: Preclinical Progress and Clinical Potential. *Nat. Rev. Cancer* **2012,** *12*, 363-368.
10. Fujimoto, J. G.; Pitris, C.; Boppart, S. A.; Brezinski, M. E., Optical Coherence Tomography: an Emerging Technology for Biomedical Imaging and Optical Biopsy. *Neoplasia (New York, NY)* **2000,** *2*, 9-25.
11. Ehlers, J. P.; Srivastava, S. K.; Feiler, D.; Noonan, A. I.; Rollins, A. M.; Tao, Y. K., Integrative Advances for OCT-guided Ophthalmic Surgery and Intraoperative OCT: Microscope Integration, Surgical Instrumentation, and Heads-up Display Surgeon Feedback. *PLoS ONE* **2014,** *9*, e105224.

12. Nguyen, F. T.; Dibbern, E. M.; Chaney, E. J.; Oldenburg, A. L.; Suslick, K. S.; Boppart, S. A. In *Magnetic Protein Microspheres As Dynamic Contrast Agents for Magnetomotive Optical Coherence Tomography*, Molecular Probes for Biomedical Applications II, International Society for Optics and Photonics: 2008; p 68670F.
13. Gao, A.; Xu, W.; Ponce de León, Y.; Bai, Y.; Gong, M.; Xie, K.; Park, B. H.; Yin, Y., Controllable Fabrication of Au Nanocups by Confined‐Space Thermal Dewetting for OCT Imaging. *Adv. Mater.* **2017,** *29*, 1701070.
14. Rao, K. D.; Choma, M. A.; Yazdanfar, S.; Rollins, A. M.; Izatt, J. A., Molecular Contrast in Optical Coherence Tomography by Use of a Pump–probe Technique. *Opt. Lett.* **2003,** *28*, 340-342.
15. John, R.; Rezaeipoor, R.; Adie, S. G.; Chaney, E. J.; Oldenburg, A. L.; Marjanovic, M.; Haldar, J. P.; Sutton, B. P.; Boppart, S. A., In Vivo Magnetomotive Optical Molecular Imaging Using Targeted Magnetic Nanoprobes. *Proc. Natl. Acad. Sci. U.S.A.* **2010,** *107*, 8085-8090.
16. Skala, M. C.; Crow, M. J.; Wax, A.; Izatt, J. A., Photothermal Optical Coherence Tomography of Epidermal Growth Factor Receptor in Live Cells Using Immunotargeted Gold Nanospheres. *Nano Lett.* **2008,** *8*, 3461-3467.
17. Wei, Q.; Song, H.-M.; Leonov, A. P.; Hale, J. A.; Oh, D.; Ong, Q. K.; Ritchie, K.; Wei, A., Gyromagnetic Imaging: Dynamic Optical Contrast Using Gold Nanostars with Magnetic Cores. *J. Am. Chem. Soc.* **2009,** *131*, 9728-9734.
18. Li, Z.; Yin, Y., Stimuli‐Responsive Optical Nanomaterials. *Adv. Mater.* **2019,** *31*, 1807061.
19. Oldenburg, A. L.; Toublan, F. J.-J.; Suslick, K. S.; Wei, A.; Boppart, S. A., Magnetomotive Contrast for In Vivo Optical Coherence Tomography. *Opt. Express* **2005,** *13*, 6597-6614.
20. Cimalla, P.; Walther, J.; Mueller, C.; Almedawar, S.; Rellinghaus, B.; Wittig, D.; Ader, M.; Karl, M. O.; Funk, R. H.; Brand, M., Improved Imaging of Magnetically Labeled Cells Using Rotational Magnetomotive Optical Coherence Tomography. *Appl. Sci.* **2017,** *7*, 444.
21. Wei, Q.; Wei, A., Optical Imaging with Dynamic Contrast Agents. *Chem. Eur. J.* **2011,** *17*, 1080-1091.
22. Lu, G. J.; Chou, L.-d.; Malounda, D.; Patel, A. K.; Welsbie, D. S.; Chao, D. L.; Ramalingam, T.; Shapiro, M. G., Genetically Encodable Contrast Agents for Optical Coherence Tomography. *ACS Nano* **2020**, *14*, 7823–7831
23. Song, G.; Kenney, M.; Chen, Y.-S.; Zheng, X.; Deng, Y.; Chen, Z.; Wang, S. X.; Gambhir, S. S.; Dai, H.; Rao, J., Carbon-coated FeCo Nanoparticles As Sensitive Magnetic-particle-imaging Tracers with Photothermal and Magnetothermal Properties. *Nat. Biomed. Eng.* **2020**, *4*, 325–334.
24. Yin, S.; Li, Z.; Cheng, L.; Wang, C.; Liu, Y.; Chen, Q.; Gong, H.; Guo, L.; Li, Y.; Liu, Z., Magnetic PEGylated Pt 3 Co Nanoparticles As a Novel MR Contrast Agent: In Vivo MR Imaging and Long-term Toxicity Study. *Nanoscale* **2013,** *5*, 12464-12473.
25. Li, Z.; Wang, C.; Cheng, L.; Gong, H.; Yin, S.; Gong, Q.; Li, Y.; Liu, Z., PEG-functionalized Iron Oxide Nanoclusters Loaded with Chlorin e6 for Targeted, NIR Light Induced, Photodynamic Therapy. *Biomaterials* **2013,** *34*, 9160-9170.
26. Vaupel, P. W.; Kelleher, D. K., Pathophysiological and Vascular Characteristics of Tumours and Their Importance for Hyperthermia: Heterogeneity Is the Key Issue. *Int. J. Hyperth.* **2010,** *26*, 211-223.

27. Jain, R. K.; Munn, L. L.; Fukumura, D., Dissecting Tumour Pathophysiology Using Intravital Microscopy. *Nat. Rev. Cancer* **2002,** *2*, 266-276.
28. Kennedy, K. M.; Chin, L.; McLaughlin, R. A.; Latham, B.; Saunders, C. M.; Sampson, D. D.; Kennedy, B. F., Quantitative Micro-elastography: Imaging of Tissue Elasticity Using Compression Optical Coherence Elastography. *Sci. Rep.* **2015,** *5*, 15538.
29. Anna, T.; Mehta, D. S.; Sato, M., Improvement of the Dynamic Range Using Background Subtraction in Single Shot Wide-field Optical Coherence Tomography. *J. Mod. Opt.* **2015,** *62*, 1816-1827.
30. Kubelick, K. P.; Mehrmohammadi, M., Magnetic Particles in Motion: Magneto-motive Imaging and Sensing. *Theranostics* **2022,** *12*, 1783.
31. Smith, B. R.; Gambhir, S. S., Nanomaterials for In Vivo Imaging. *Chem. Rev.* **2017,** *117*, 901-986.
32. Li, Z.; Wang, M.; Zhang, X.; Wang, D.; Xu, W.; Yin, Y., Magnetic Assembly of Nanocubes for Orientation-dependent Photonic Responses. *Nano Lett.* **2019,** *19*, 6673-6680.
33. Xu, W.; Wang, M.; Li, Z.; Wang, X.; Wang, Y.; Xing, M.; Yin, Y., Chemical Transformation of Colloidal Nanostructures with Morphological Preservation by Surface-protection with Capping Ligands. *Nano Lett.* **2017,** *17*, 2713-2718.
34. Li, Z.; Yin, S.; Cheng, L.; Yang, K.; Li, Y.; Liu, Z., Magnetic Targeting Enhanced Theranostic Strategy Based on Multimodal Imaging for Selective Ablation of Cancer. *Adv. Funct. Mater.* **2014,** *24*, 2312-2321.
35. Li, Z.; Myung, N. V.; Yin, Y., Light-powered Soft Steam Engines for Self-adaptive Oscillation and Biomimetic Swimming. *Sci. Robot.* **2021,** *6*, eabi4523.
36. Li, Z.; Zhang, J.; Jin, J.; Yang, F.; Aleisa, R.; Yin, Y., Creation and Reconstruction of Thermochromic Au Nanorods with Surface Concavity. *J. Am. Chem. Soc.* **2021,** *143*, 15791-15799.
37. Li, Z.; Yang, F.; Yin, Y., Smart Materials by Nanoscale Magnetic Assembly. *Adv. Funct. Mater.* **2020,** *30*, 1903467.
38. Wang, M.; Yin, Y., Magnetically Responsive Nanostructures with Tunable Optical Properties. *J. Am. Chem. Soc.* **2016,** *138*, 6315-6323.
39. Li, Z.; Fan, Q.; Yin, Y., Colloidal Self-assembly Approaches to Smart Nanostructured Materials. *Chem. Rev.* **2021,** *122*, 4976–5067.
40. Wang, X.; Feng, J.; Yu, H.; Jin, Y.; Davidson, A.; Li, Z.; Yin, Y., Anisotropically Shaped Magnetic/plasmonic Nanocomposites for Information Encryption and Magnetic-field-direction Sensing. *Research* **2018,** *2018*, 7527825.
41. Wang, M.; He, L.; Xu, W.; Wang, X.; Yin, Y., Magnetic Assembly and Field‐tuning of Ellipsoidal‐nanoparticle‐based Colloidal Photonic Crystals. *Angew. Chem. Int. Ed.* **2015,** *54*, 7077-7081.
42. Li, Z.; Fan, Q.; Wu, C.; Li, Y.; Cheng, C.; Yin, Y., Magnetically Tunable Plasmon Coupling of Au Nanoshells Enabled by Space-free Confined Growth. *Nano Lett.* **2020,** *20*, 8242-8249.
43. Chang, W.-S.; Ha, J. W.; Slaughter, L. S.; Link, S., Plasmonic Nanorod Absorbers As Orientation Sensors. *Proc. Natl. Acad. Sci. U.S.A.* **2010,** *107*, 2781-2786.
44. Liu, Q.; Yuan, Y.; Smalyukh, I. I., Electrically and Optically Tunable Plasmonic Guest–host Liquid Crystals with Long-range Ordered Nanoparticles. *Nano Lett.* **2014,** *14*, 4071-4077.

45. Ji, T.; Lirtsman, V. G.; Avny, Y.; Davidov, D., Preparation, Characterization, and Application of Au‐Shell/Polystyrene Beads and Au‐Shell/Magnetic Beads. *Adv. Mater.* **2001,** *13*, 1253-1256.
46. Smith, A. M.; Mancini, M. C.; Nie, S., Bioimaging: Second Window for In Vivo Imaging. *Nat. Nanotechnol.* **2009,** *4*, 710.
47. Geddes, L. A.; Baker, L. E., The Specific Resistance of Biological Material—a Compendium of Data for the Biomedical Engineer and Physiologist. *Med. Biol. Eng.* **1967,** *5*, 271-293.
48. Chhetri, R. K.; Blackmon, R. L.; Wu, W.-C.; Hill, D. B.; Button, B.; Casbas-Hernandez, P.; Troester, M. A.; Tracy, J. B.; Oldenburg, A. L., Probing Biological Nanotopology via Diffusion of Wweakly Constrained Plasmonic Nanorods with Optical Coherence Tomography. *Proc. Natl. Acad. Sci. U.S.A.* **2014,** *111*, E4289-E4297.
49. Zaki, F.; Wang, Y.; Su, H.; Yuan, X.; Liu, X., Noise Adaptive Wavelet Thresholding for Speckle Noise Removal in Optical Coherence Tomography. *Biomed. Opt. Express* **2017,** *8*, 2720-2731.
50. Watson, J. H.; Cardell, R.; Heller, W., The Internal Structure of Colloidal Crystals of β-FeOOH and Remarks on Their Assemblies in Schiller Layers. *J. Phys. Chem.* **1962,** *66*, 1757-1763.
51. Huang, Y.; Ishige, R.; Tsujii, Y.; Ohno, K., Synthesis of Iron Oxide Rods Coated with Polymer Brushes and Control of Their Assembly in Thin Films. *Langmuir* **2015,** *31*, 1172-1179.

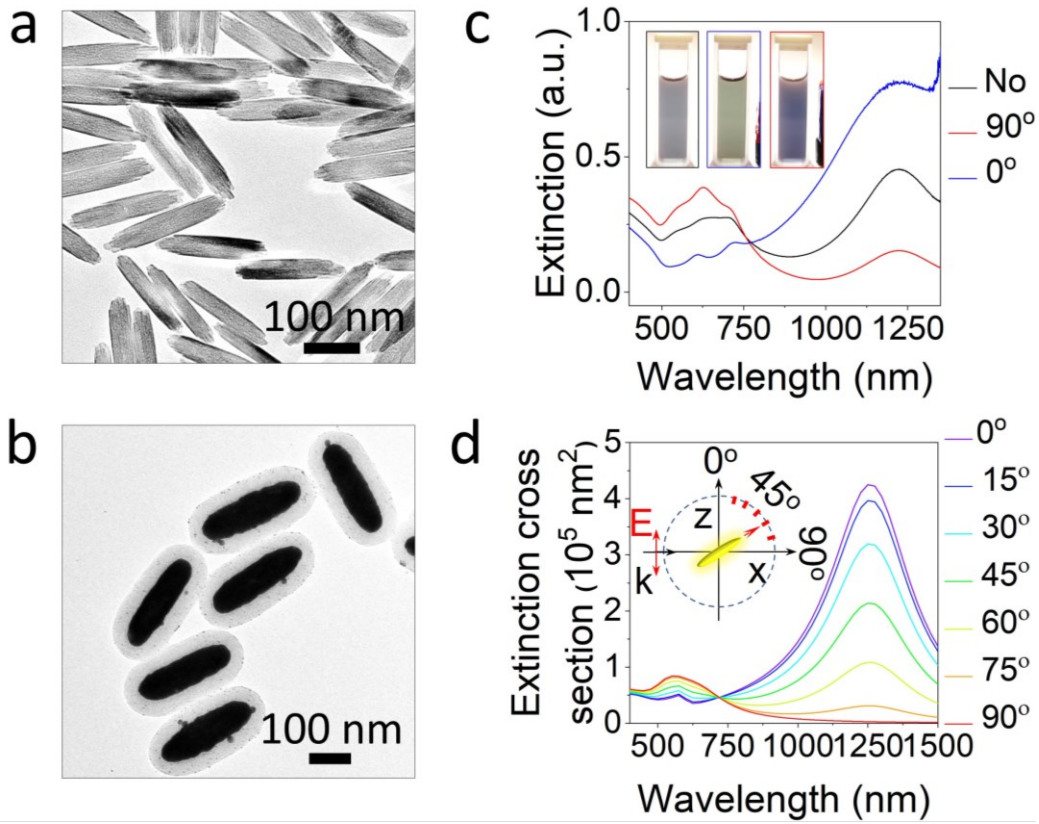


**Figure 1.** TEM images of (a) FeOOH nanorods and (b) $Fe_3O_4$@Au@RF nanorods. (c) Extinction spectra of $Fe_3O_4$@Au@RF nanorods measured under polarized light. The angles indicate the angle between the direction of the applied magnetic field and the polarization of incident light. (d) Calculated extinction cross-section of Au shells under different orientations as indicated in the inset.

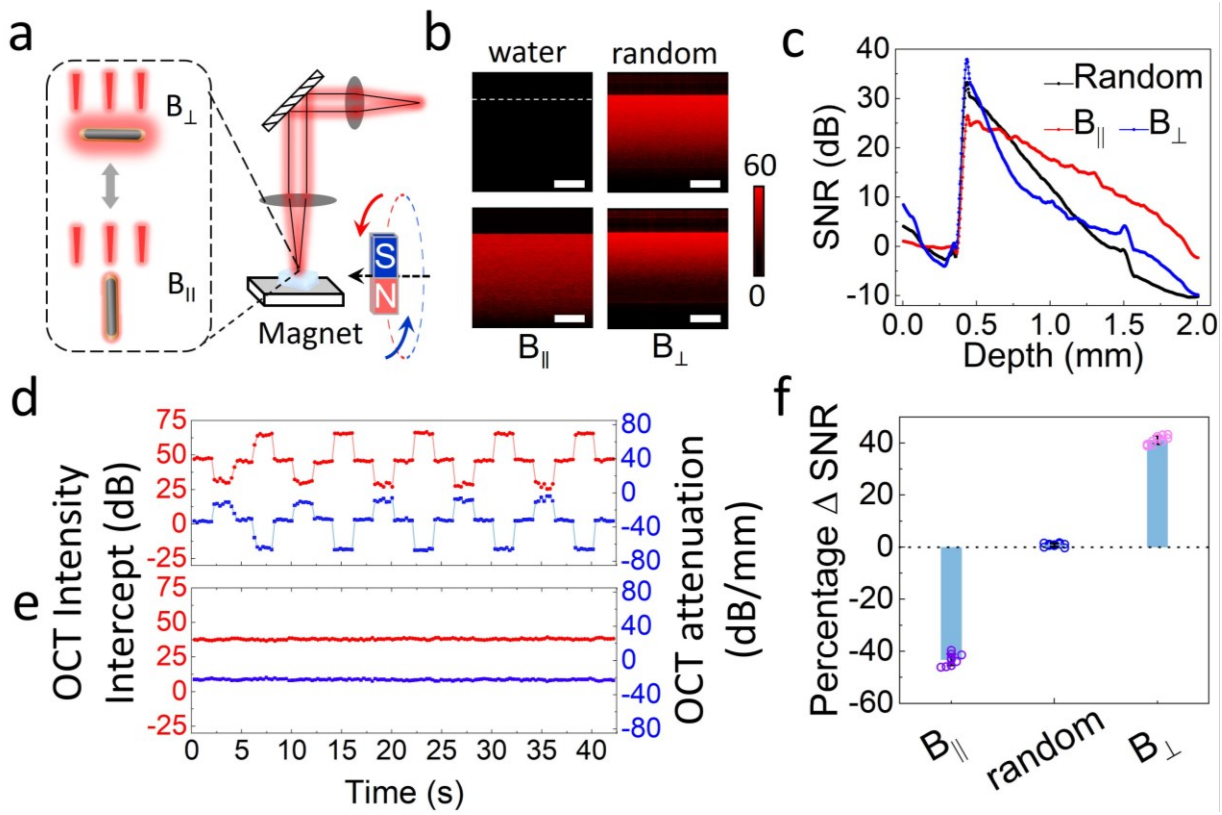


**Figure 2.** (a) Magnetically modulated dynamic OCT imaging using $Fe_3O_4$@Au@RF nanorods as the contrast agent. (b) OCT images of water and colloidal dispersions of $Fe_3O_4$@Au@RF nanorods with and without magnetic fields. Scale bars: 0.5 mm. The color bar represents the signal intensity in the dB scale with the noise floor set to 0. (c) Line profile of SNR of the OCT images modulated by different magnetic fields. (d, e) Tunability and changes (bottom panel) of OCT intensity (signal noise above sample normalized to 0 dB) modulated by magnetic fields of (d) $Fe_3O_4$@Au@RF and (e) FeOOH@Au@RF. (d) and (e) share the same x-axis. (f) Percentage of SNR changes of OCT images in response to an external magnetic field.

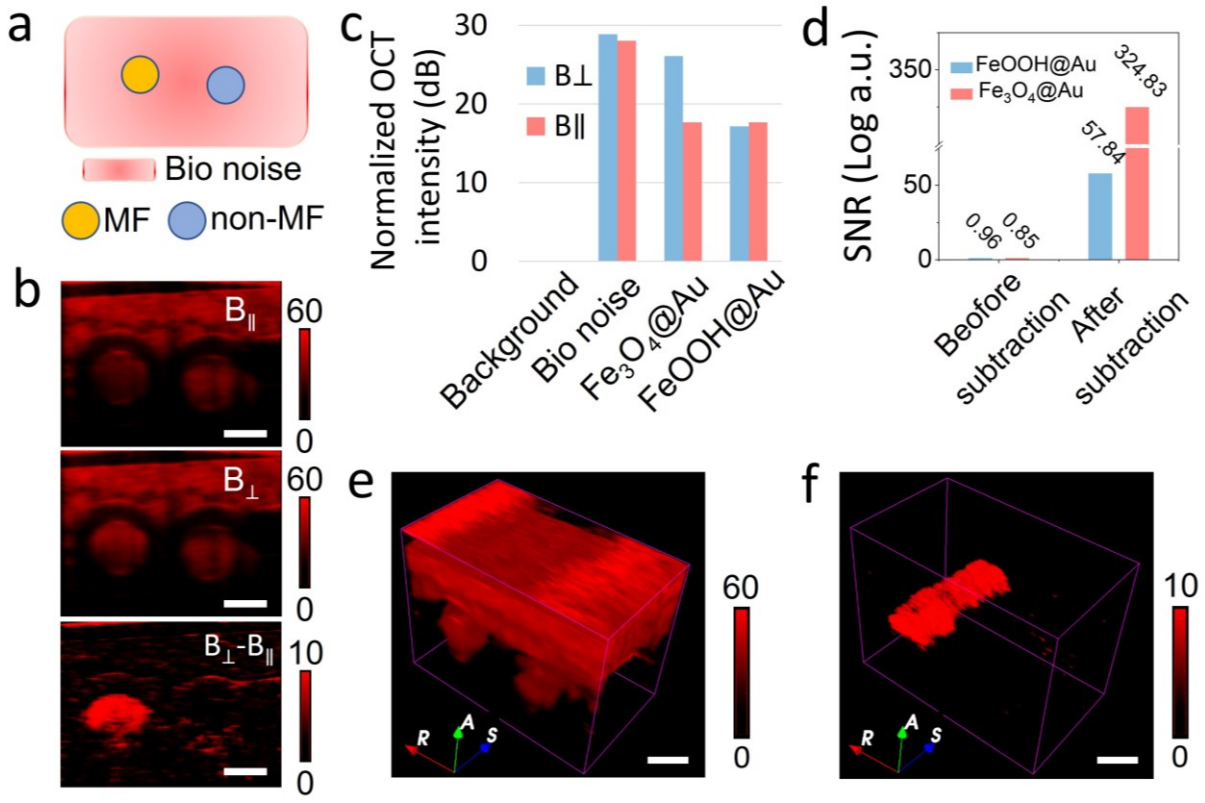


**Figure 3.** (a) Scheme of ex vivo phantom used for biological imaging. The Bio noise, MF, and non-MF represent biological noise, magnetic field-responsive ($Fe_3O_4$@Au) nanorods, and non-responsive (FeOOH@Au) nanorods, respectively. (b) Ex vivo OCT imaging. Scale bars: 2 mm. (c) OCT signal changes modulated by magnetic fields. Data normalized to background noise in air above the sample. (d) Enhancement of SNR (logarithmic arbitrary units) in OCT imaging enabled by magnetic alignment. (e) 3D rendering of OCT imaging under perpendicular magnetic fields. (f) 3D rendering of background-free OCT imaging enabled by magnetic modulation and pixel subtraction. Scale bars in (e) and (f): 2 mm.

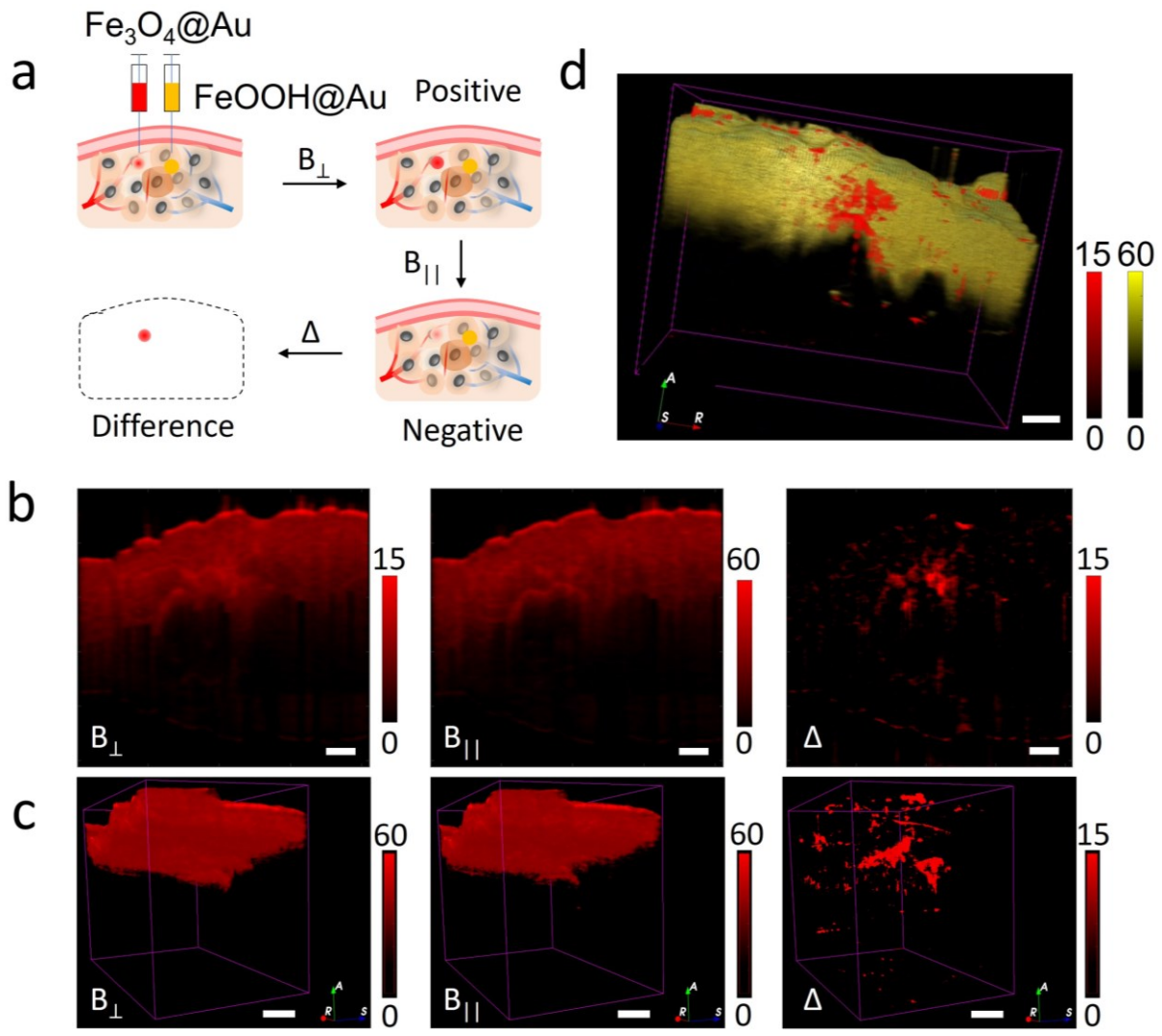


**Figure 4.** (a) Schematic illustration of NIR-II background-free OCT imaging. (b) In vivo 2D OCT imaging. OCT intensity normalized to noise in air above the sample. (c) 3D rendering of OCT imaging. (d) Reconstructed OCT image volume. The signal from the imaging contrast agent is in red, while the background OCT signal is in yellow. Scale bars in (b), (c) and (d): 1 mm.

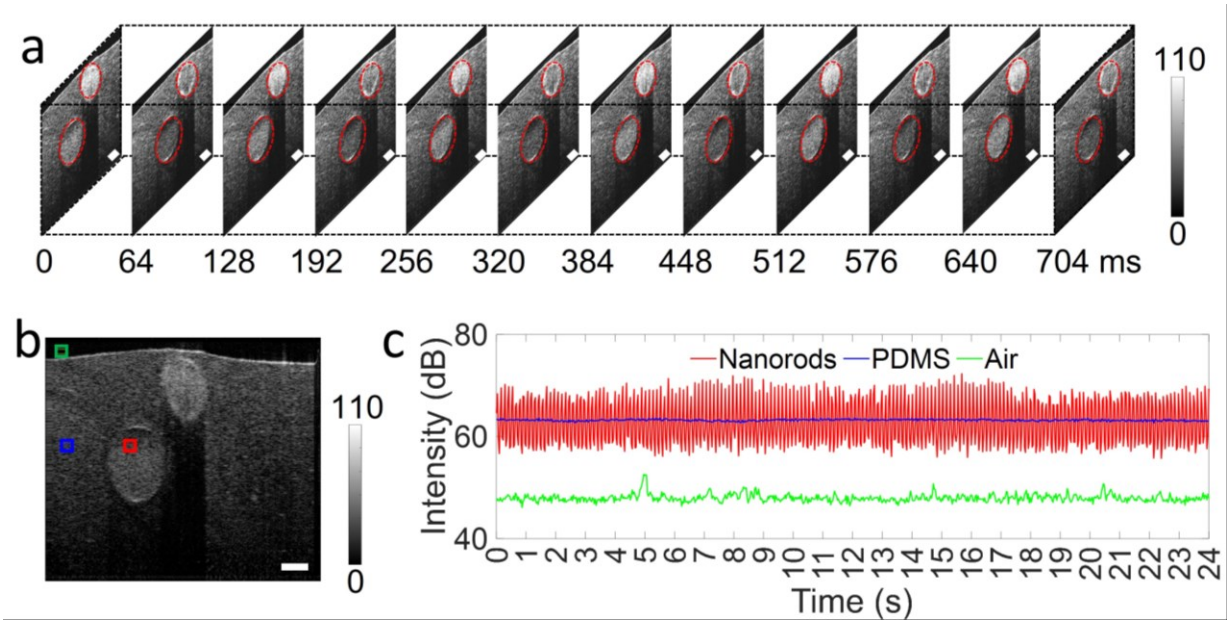


**Figure 5.** Ex vivo FFT-processed background-free imaging. (a) Magnetic field-modulated real-time OCT images. The regions with responsive OCT signals are highlighted in red dashed circles. (b) One typical OCT image shows the regions to acquire OCT signals. Red, blue, and green boxes indicate the nanorod, PDMS, and air regions, respectively. Scale bars in (a) and (b): 1 mm. (c) Real-time OCT signals in dB scale in the regions as shown in (b). The OCT signals presented in (c) are from the regions labeled with the same colors in (b). The alternating frequency of the applied magnetic field is 4 Hz.

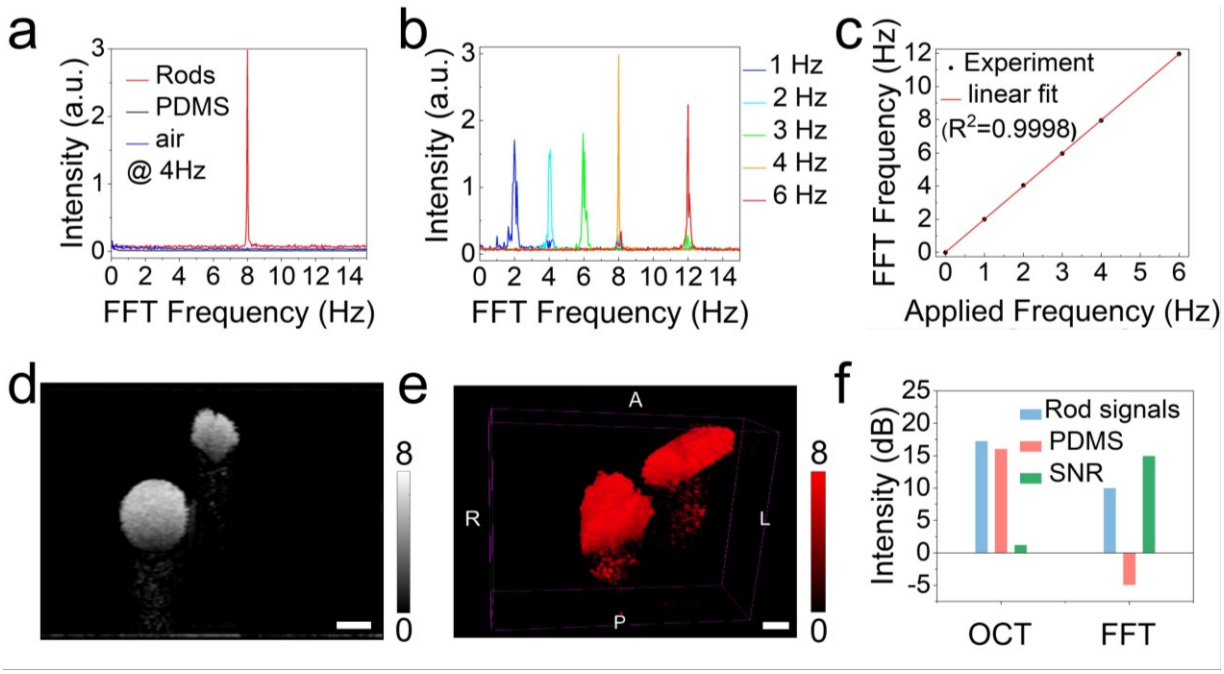


**Figure 6.** Ex vivo FFT-processed background-free imaging. (a) FFT signals of the real-time OCT intensity of rods, PDMS, and air. (b) FFT signals of rods in the phantom when the frequency of applied magnetic fields increased from 1Hz to 12 Hz. (c) Correlation between the calculated FFT frequency and the applied frequency of the magnetic fields. (d) One slice of OCT image created by the FFT-processed imaging technique. (e) 3D volume rendering of the FFT-processed background-free imaging. (f) The SNR in the conventional and FFT-processed OCT imaging technique. Scale bars in (d) and (e): 1 mm.

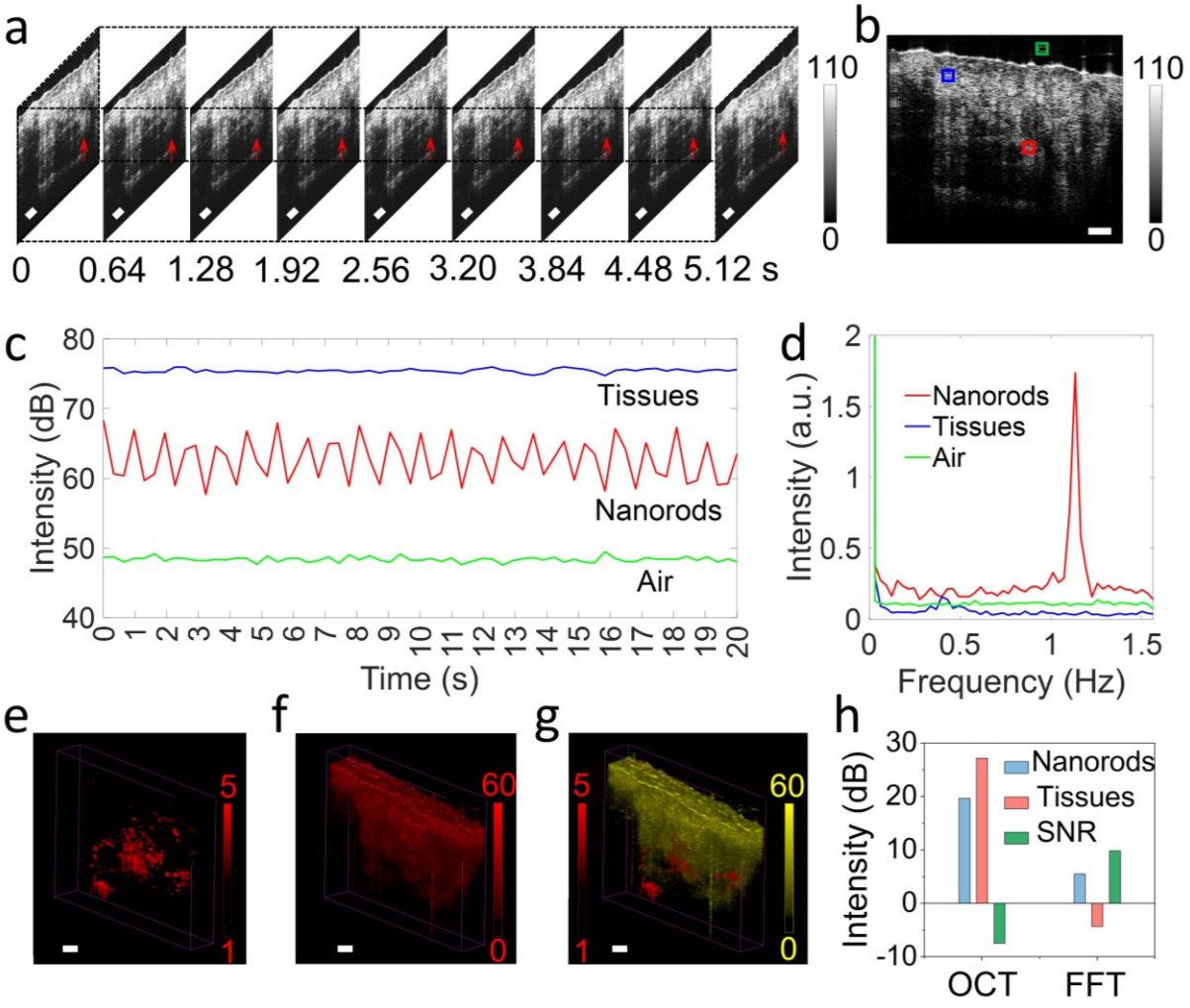


**Figure 7**. In vitro FFT-processed background-free imaging. (a) Magnetic field-modulated real-time OCT images in pork tissue after being injected with rods. (b) One typical OCT image shows the regions to acquire OCT signals. Red, blue, and green boxes indicate the injected nanorod, background tissue, and air regions, respectively. (c) Real-time OCT signals in dB scale in the regions as shown in (b). The OCT signals presented in (c) are from the regions labeled with the same colors in (b). (d) FFT singles of the real-time OCT intensity of rods (red), tissues (blue), and air (yellow). 3D volume rendering of specific rod signals (e), biological backgrounds (f), and the merged images (g) after FFT processing. (h) The SNR in the conventional and FFT-processed OCT imaging in the biological tissues. Scale bars in (a), (b), (e), (f) and (g): 1 mm.

TOC Graphic: